An Investigation of Underwater Sound Propagation from Pile Driving

WA-RD 781.1

Per G. Reinhall
Peter H. Dahl

December 2011

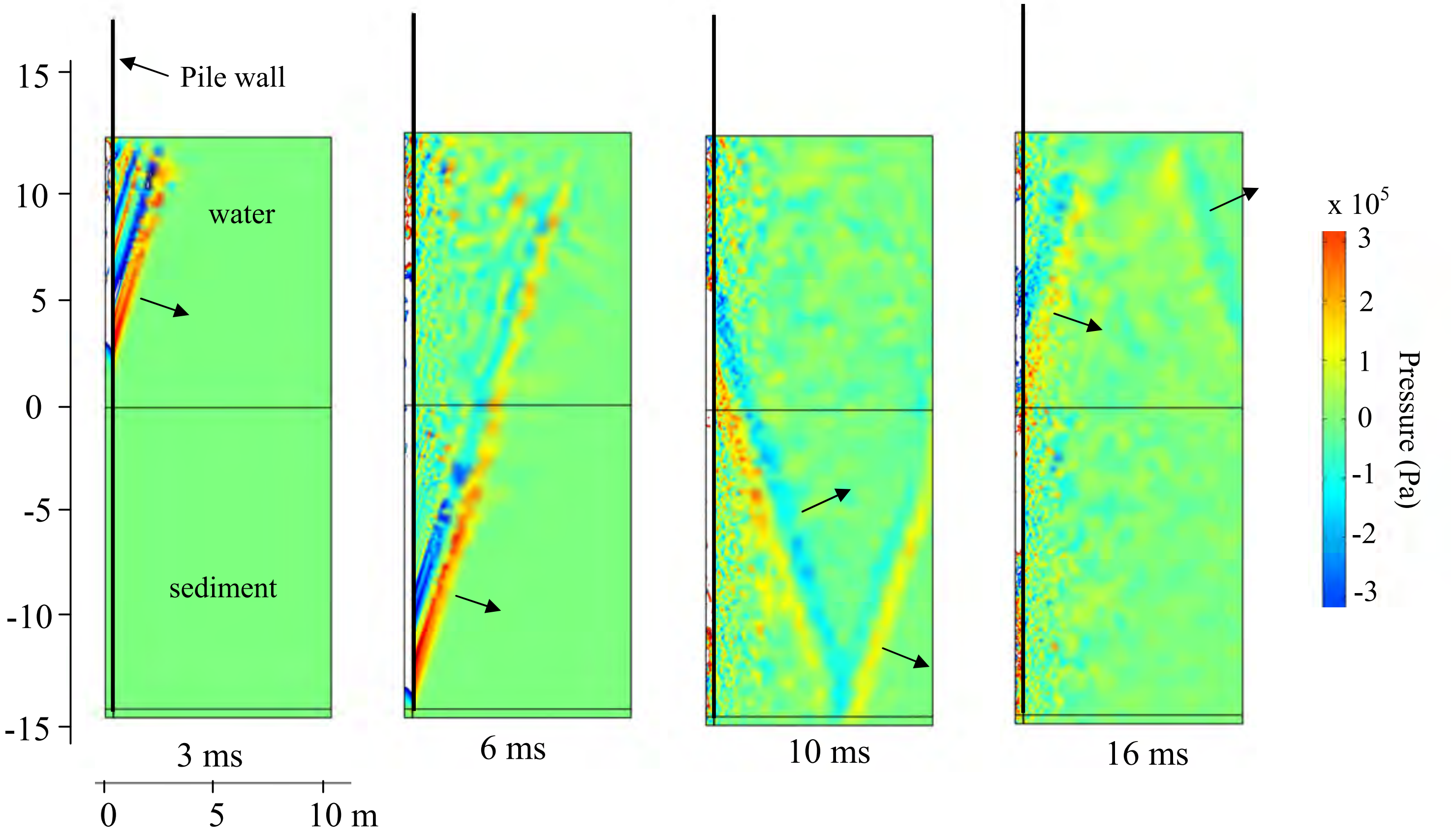

Washington State Department of Transportation
Office of Research & Library Services

WSDOT Research Report

RESEARCH REPORT
Agreement T4118, Task 43
Underwater Sound

AN INVESTIGATION OF UNDERWATER SOUND PROPAGATION FROM PILE DRIVING

by

Per G. Reinhall
Professor
Department of Mechanical Engineering
University of Washington, Box 352600
Seattle, Washington 98195

Peter H. Dahl
Professor
Applied Physics Laboratory
University of Washington, Box 355640
Seattle, Washington 98195

Washington State Transportation Center (TRAC)
University of Washington, Box 354802
1107NE 45th Street, Suite 535
Seattle, Washington 98105-4631

Washington State Department of Transportation Technical Monitors
Marion Carey, Jim Laughlin
Environmental Services Department
Rick Huey
Washington State Ferries

Prepared for
The State of Washington
Department of Transportation
Paula J. Hammond, Secretary

December 2011

TECHNICAL REPORT STANDARD TITLE PAGE

1. REPORT NO. WA-RD 781.1	2. GOVERNMENT ACCESSION NO.	3. RECIPIENT'S CATALOG NO.
4. TITLE AND SUBTITLE AN INVESTIGATION OF UNDERWATER SOUND PROPAGATION FROM PILE DRIVING		5. REPORT DATE December 2011 6. PERFORMING ORGANIZATION CODE
7. AUTHORS Per G. Reinhall and Peter H. Dahl		8. PERFORMING ORGANIZATION CODE
9. PERFORMING ORGANIZATION NAME AND ADDRESS Washington State Transportation Center University of Washington, Box 354802 University District Building, 1107 NE 45th Street, Suite 535 Seattle, Washington (98105-7370)		10. WORK UNIT NO. 11. CONTRACT OR GRANT NUMBER Agreement T4118, Task 43
12. SPONSORING AGENCY NAME AND ADDRESS Research Office Washington State Department of Transportation Transportation Building, MS 47372 Olympia, Washington 98504-7372 Project Manager: Rhonda Brooks, 360-705-7946		13. TYPE OF REPORT AND PERIOD COVERED Research Report 14. SPONSORING AGENCY CODE
15. SUPPLIMENTARY NOTES		

16. ABSTRACT

The underwater noise from impact pile driving was studied by using a finite element model for the sound generation and a parabolic equation model for propagation. Results were compared with measurements taken with a vertical line array deployed during tests at the Vashon Island ferry terminal near Seattle in November 2009. Tests showed that the dominant underwater noise produced by impact driving is from the Mach wave associated with the radial expansion of the pile that propagates down the pile after impact at supersonic speed.

The effectiveness of surrounding the pile in the water with a double-walled steel tube, also called a temporary noise attenuation pile (TNAP), to reduce the underwater sound caused by pile driving operations was also investigated. Tests and analysis showed that the noise attenuation capability of the TNAP was limited to approximately 10 dB because of the unconstrained propagation of Mach waves directly from the sediment into the water.

17. KEY WORDS Pile driving, impact, acoustics, underwater noise, attenuation, propagation			18. DISTRIBUTION STATEMENT
19. SECURITY CLASSIF. (of this report)	20. SECURITY CLASSIF. (of this page)	21. NO. OF PAGES	22. PRICE

DISCLAIMER

Table of Contents

Section *Page*

FIGURES

Figure *Page*

1. INTRODUCTION

Pile driving in water produces extremely high sound levels in both the surrounding air and underwater environments. In terms of the underwater environment, field observations show peak acoustic pressures of $\sim 10^3$ Pa measured (de Jong and Ainslie 2008) at a range of 3000 m, $\sim 10^4$ Pa measured (Robinson et al. 2007) at a range of 60 m, and $\sim 10^5$ Pa measured (this work) at a range of 10 m from the pile driving operation. Such pressures are known to produce deleterious effects on both fish and marine mammals (Madsen et al. 2006). As a result, pile driving has become a highly regulated construction process with significant environmental monitoring costs. Still, beyond measurements of peak and other integral measures of pressure and related energy spectra, relatively little is known about the process of underwater sound generation and propagation from pile driving, such as acoustic field variation with water depth and distribution in vertical angle.

In this report we present the results of a simulation and measurement of underwater noise generated by the impact driving of both bare (untreated) piles and piles surrounded by a double-walled steel tube, also called a temporary noise attenuation pile (TNAP). The researchers conducted a full structural acoustic simulation with finite element (FE) techniques and a parabolic wave equation (PE) simulation within a shallow water waveguide with a vertical distribution of phased point sources, as suggested by the FE results. The measurements, involving a vertical line array of hydrophones, were from a full-scale pile driving test carried out at the Vashon Island ferry terminal near Seattle, Washington, in November 2009.

2. UNTREATED PILES

Tests showed that the primary source of underwater sound is compression of the pile during pile driving. The hammer strike produces a compression wave in the pile and an associated radial displacement motion due to the effect of Poisson’s ratio of steel. When the pile is surrounded by water, the speed of the downward traveling radial displacement wave (~5015 m/s) in the pile is higher than the speed of sound in the water. This produces an acoustic field in the shape of an axisymmetric cone, or Mach cone. The essential properties of the Mach cone were subsequently verified by the measurements from a vertical line array. Of course, other factors contribute to the underwater noise field associated with pile vibrations. But it is the field associated with this Mach cone that clearly dominates peak pressure.

In this section we present results from the finite element modeling of impact pile driving. Field measurements taken from a full-scale pile driving experiment are presented that relate directly to predictions made by the FE analysis. We also present the results of a companion modeling effort based on the parabolic wave equation (PE) approach, with additional comparisons to the field data.

2.1. Finite Element Analysis

To investigate the acoustic radiation due to a pile strike, we created a dynamic axisymmetric finite element model of a pile being driven into the sediments in shallow water by using an implicit finite element code (Comsol Multiphysics). The model was made to be consistent with one of the four piles of the 2009 Vashon Island ferry terminal test: a hollow steel pile, approximately 32 m (105 m) long with a 76.2-cm (30-in.) diameter and wall thickness of 2.54 cm (1 in.). The pile was driven approximately 14 m into the sediment in water 12.5 m deep. Cylindrical domains of water and sediment with radii of 10 m were included in the finite element model (see Figure 1). Perfectly matched boundary conditions were used to prevent reflections from the artificial boundaries that truncated these domains. The pile was fluid-loaded via interaction between the water and the sediment and was discretized by using approximately 20,100 quadratic quadrilateral Lagrange elements with an element size of 6.3 mm. The water and sediment were discretized by using approximately 151,000 quadratic triangular elements. The wave propagation in the pile and the surrounding medium was modeled for 20 ms by using a typical time step of 0.02 μs.

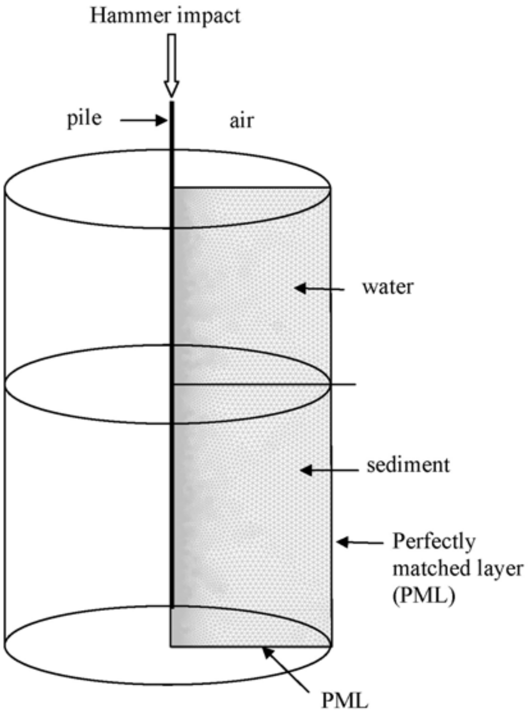

Figure 1. Axisymmetric finite element model of pile and water.

The Vashon piles were driven with a Delmag D62-22 Diesel Hammer with an impact weight of 6,200 kg and energy of 180 kNm. No cushion between the weight and pile was used. The approximate pressure, $p(t)$, resulting from the impact between the hammer weight and the pile was determined by an axisymmetric finite element impact analysis. For this purpose, the effect of the water and sediment was assumed to be negligible, and only the hammer weight and the pile were modeled by using quadrilateral Lagrange elements without taking the fluid structure into account. The impact weight was set to have an initial downward velocity of 7.6 m/s. Tests determined that the average pressure across the top of the pile during impact could be approximated by the equation $p(t) = 2.1\ 10^8\ exp(-t/\tau)$ Pa, where t is time after impact in seconds and the time constant τ is equal to 0.004s. Note that rise time in stress at the interface after impact was several orders of magnitude smaller than the time constant τ, so the pressure was assumed to experience a step change at the moment of impact followed by exponential decay. This was consistent with previously published data from strain gage measurements (Fellenius 1996). The water sound speed, c_w, was set to 1485 m/s, and the sediment was modeled as a fluid with a sound speed, c_s, equal to 1625 m/s. Additional remarks on sediment modeling are given in Section 2.3.

The compression wave in the pile caused by the hammer strike at the top of the pile produced a local radial deformation due to a Poisson's ratio effect (Poisson's ratio for steel is approximately 0.3). This radial deformation propagated downwards along the pile with the longitudinal wave at a speed of c_p = 5,015 m/s along the section of the pile that was surrounded by water. The axial stress wave in the pile produced by the hammer impact created a spike in the radial velocity followed by oscillation of the pile wall after the initial wave had passed through. The propagating velocity spike produced a similar spike in the acoustic pressure along the pile wall. Figure 2 shows this pressure spike at 3 and 6 ms after impact at a range of 1 m from the pile wall. As an aside, we noted that the negative pressure spike initially exceeded a nominal cavitation pressure threshold that varied with depth (thin dashed line); however, the pressures were also of short duration, which is known to increase this threshold (Weston 1960).

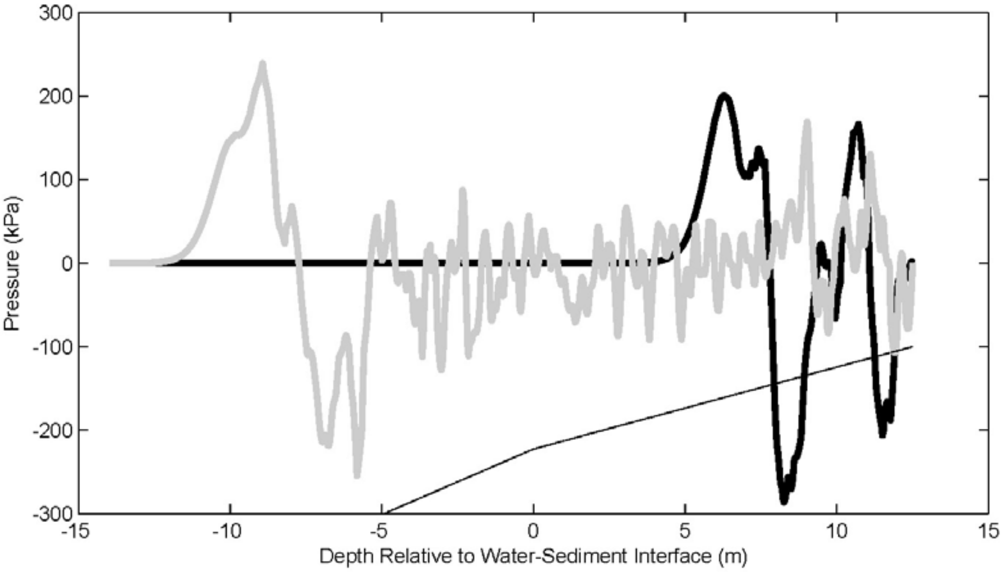

Figure 2. Acoustic pressure along the pile at a range of 1 m from the pile wall at 3 ms (black line) and 6 ms (gray line). The water surface is at z = 12.5 m. The nominal depth-dependent cavitation threshold is shown by the thin line, although the actual threshold was likely higher because of the short duration of the pressures.

Figure 3 shows an axisymmetric surface plot of the total acoustic pressure at 3, 6, 10, and 16 ms after impact. The supersonic (relative to the water) radial displacement wave in the pile produced an acoustic field in the water in the shape of an axisymmetric cone, or Mach cone, with its apex traveling along with the pile deformation wave front. As can be seen in Figure 3, the initial Mach cone was followed by weaker alternating pressure variations due to oscillations of the pile wall. The radial deformation in the pile and the apex of the Mach cone reached the bottom end of the pile approximately 6 ms after impact. Note that the perfectly matched boundary conditions prevented any significant reflections from boundaries of the truncated fluid and sediment regions.

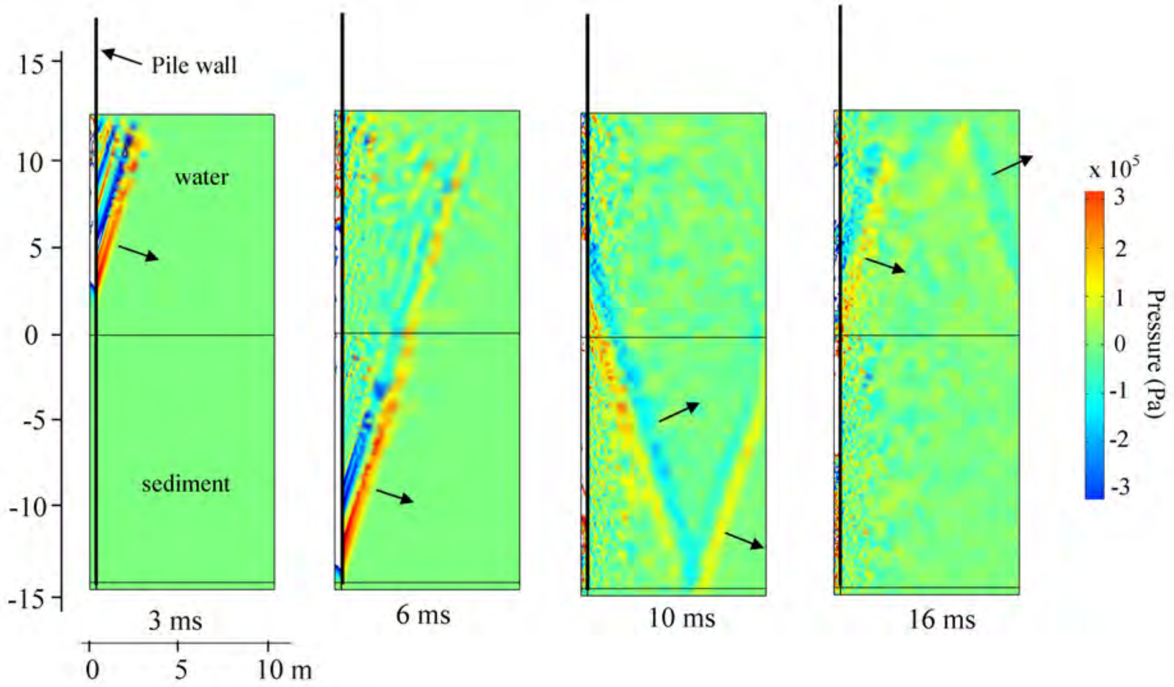

Figure 3. Acoustic pressure surface plots showing the acoustic radiation from the pile after 3, 6, 10, and 16 ms after impact by the pile hammer. The propagation directions of the wave fronts associated with the Mach cones produced in the water and the sediment are indicated by the arrows.

A schematic of the results is shown in Figure 4 to clarify the chain of events and to show the speeds and angles of the propagation of the Mach cones. In the figure, the first Mach cone is formed with a cone angle of $\varphi_w = \sin^{-1}(c_w / c_p) = 17.2^\circ$. Note that this is the angle between the vertically oriented pile and the wave front associated with the Mach cone. This angle depends only on the two wave speeds and is independent of the distance from the pile. The Mach cone angle changed from φ_w to $\varphi_s = \sin^{-1}(c_s / c_p) = 18.6^\circ$ as the pile bulge wave entered the section of the pile that was surrounded by sediment. Note that the pile bulge wave speed, c_p, in the sediment was slightly higher than that in water because of the higher bulk modulus of the sediment and was equal to 5082 m/s.

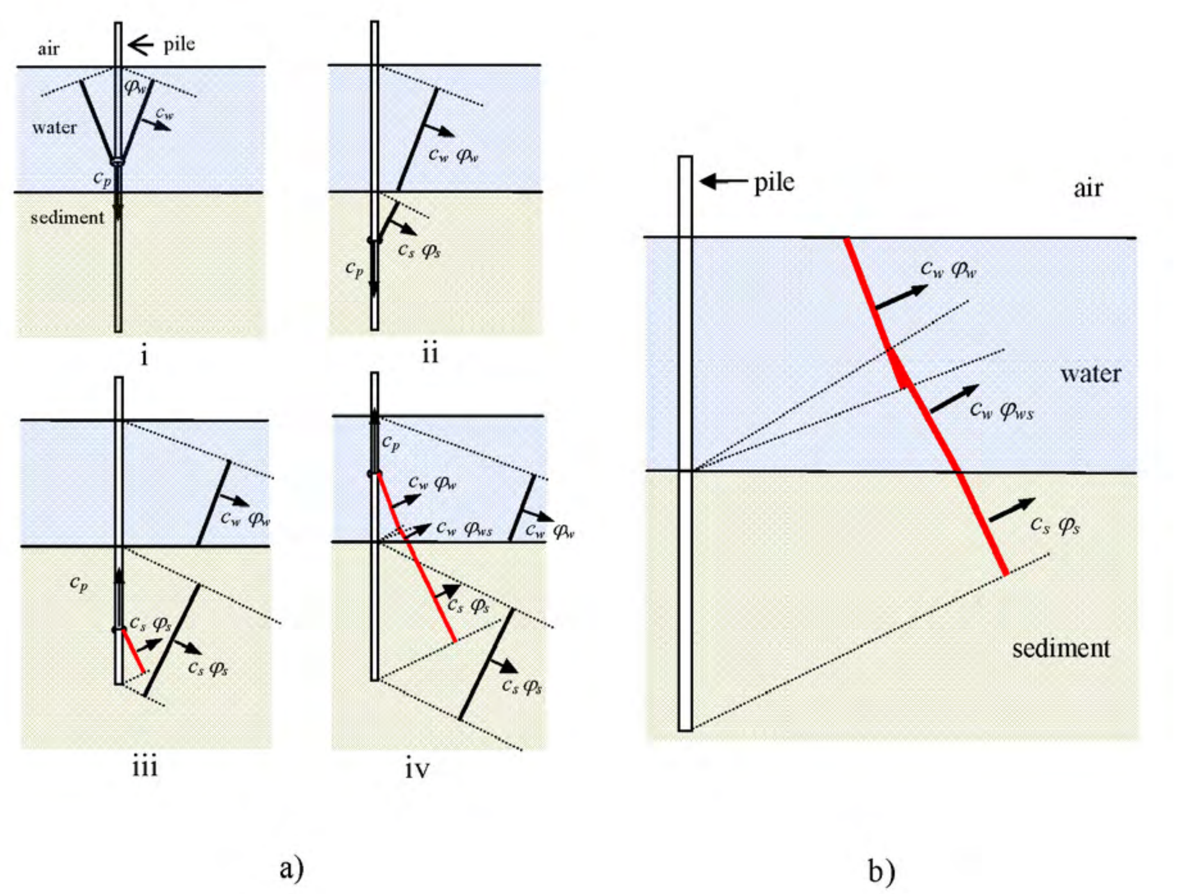

Figure 4. (a) Illustration of the propagation of the primary wave fronts associated with the Mach cone generated by the pile compression wave. i) Wave fronts before reaching the sediment. ii) Wave fronts after pile deformation wave has reached the sediment. iii) Wave fronts after the first reflection of deformation wave. iv) Wave fronts after the reflected deformation wave has reached the water.
(b) Illustration showing only the first upward traveling wave fronts after the deformation wave has reached the top of the pile.

As the deformation wave reached the bottom end of the pile (approximately 6 ms after impact), it was reflected upwards because there was an impedance mismatch between the pile and the sediment. This reflected wave in turn produced an upward moving Mach cone of angle φ_s. The sound field associated with this cone propagated up through the sediment and penetrated into the water, whereupon φ_s changed to $\varphi_{ws} = 30.0^o$ following Snell's law. Ultimately, two upward moving wave fronts occurred in the water, as shown in the schematic in Figure 4b. One had an angle of φ_{ws} and one had an angle of φ_w, the latter produced directly by the upward moving pile wave front in the water.

Note from figures 3 and 4 that the primary influence of the downward moving Mach cone will not be seen in depths of less than D^*, where $D^* \approx R \tan\varphi_w$, and R is the horizontal range from the pile source. Furthermore, the sediment-reflected wave front is significantly weaker than the incident Mach cone and cannot be observed in depths of greater than D^*. There is, however, a contribution from the upward moving Mach cone within this region. These observations are important, as this means that the reach of the initial and strongest acoustic wave that is associated with the downward moving Mach cone is limited to a range equal to about R^*, where $R^* \approx D / \tan\varphi_w$ and D is water depth. This will be discussed further in Section 2.3.

2.2 Observations (1): Time Series and Vertical Arrival Angle

An experiment to measure underwater noise from pile driving was conducted at the Washington State Ferries Vashon Island ferry terminal in November 2009 as part of a planned terminal construction project. The piles described in Section 2.1 were installed in waters 12.5 m deep (depending somewhat on tidal range). Underwater sound measurements were taken with a vertical line array (VLA) consisting of nine hydrophones (ITC 1042) spaced 0.7 m apart, with the lowest hydrophone placed 2 m above the seabed (Figure 5). The VLA was positioned 8, 12, and 15 m from the pile installation site, depending on the particular test.

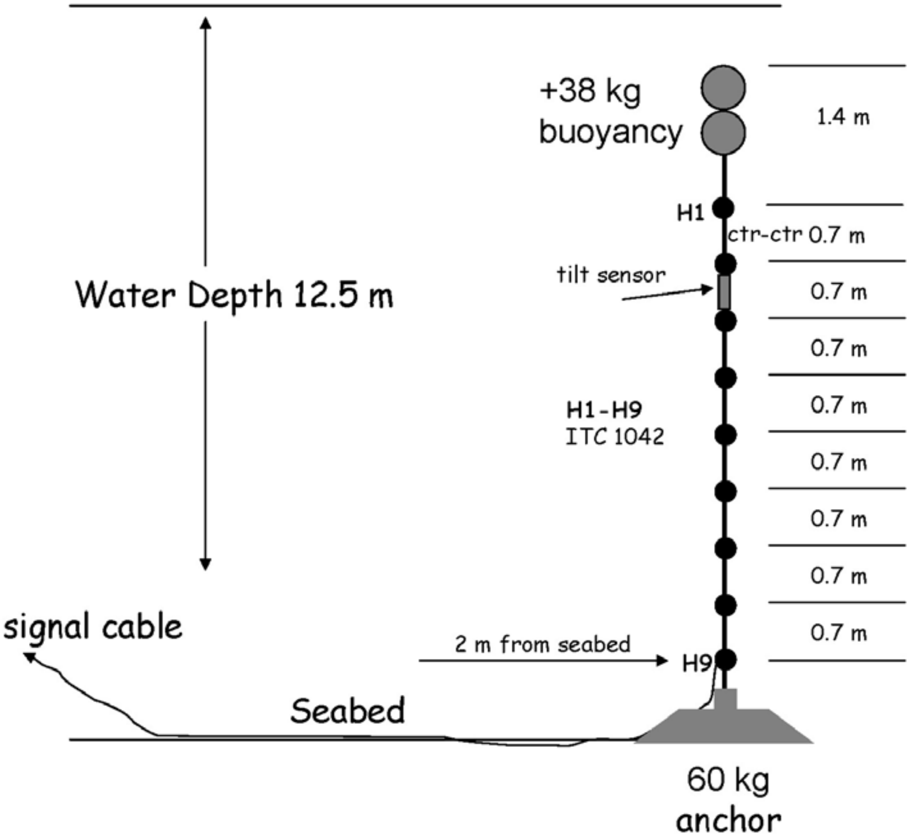

Figure 5. Vertical line array used for measuring underwater acoustic radiation from impact installation pile driving

Acoustic data were recorded at a sample rate of 62,500 Hz, with a hydrophone receiving sensitivity equal to -210 dB re V/μPa (+/- 1.5 dB) without pre-amplification to avoid system network saturation from the expected high-level inputs. A pressure time series (gray lines, Figure 6) recorded by two of the vertically separated hydrophones showed acoustic pressure originating from a pile driven by a 6,200 kg impact hammer at a range of 12 m from the VLA. (The data were a coherent average from 20 pile strikes that were remarkably consistent.) For reference, the horizontal dotted lines in Figure 6 show where pressure amplitude exceeded 210 dB re 1 μPa. The effective duration of the data was 15 ms, and this was roughly divided into three phases associated with the downward and upward Mach cones. The pressure from the first and highest amplitude downward Mach cone (phase-1) is identified by the thin black line (label 1 in Figure 6) plotted over the data for each receiver. Shallow receivers on the VLA detected this phase first, and the temporal lag, ~0.5 ms, between these two vertically separated receivers suggested a vertical arrival angle (discussed further below). Next, pressure from the first upward Mach cone (phase-2) originating from the reflection at the end of the pile is identified in the figure by the thick black line (label 2) also plotted over the data; deeper receivers detected this first. We inferred from both the FE analysis results in Section 2.1 and the field observations discussed here that this process repeated. Specifically, a phase-3 (label 3) is shown that is smaller in amplitude than phase-1 but otherwise has the same positive-to-negative development in the pressure wave. Scaled versions of phase-1 (dashed line) are plotted over the data from each receiver at delay T sec. after the onset of phase-1 for each receiver, where T represents the nominal travel time of the bulge wave over twice the length of the pile. In Figure 6, T is 12.6 ms, which puts c_p ~ 5,080 m/s or quite consistent with that predicted by the FE analysis in Section 2.1.

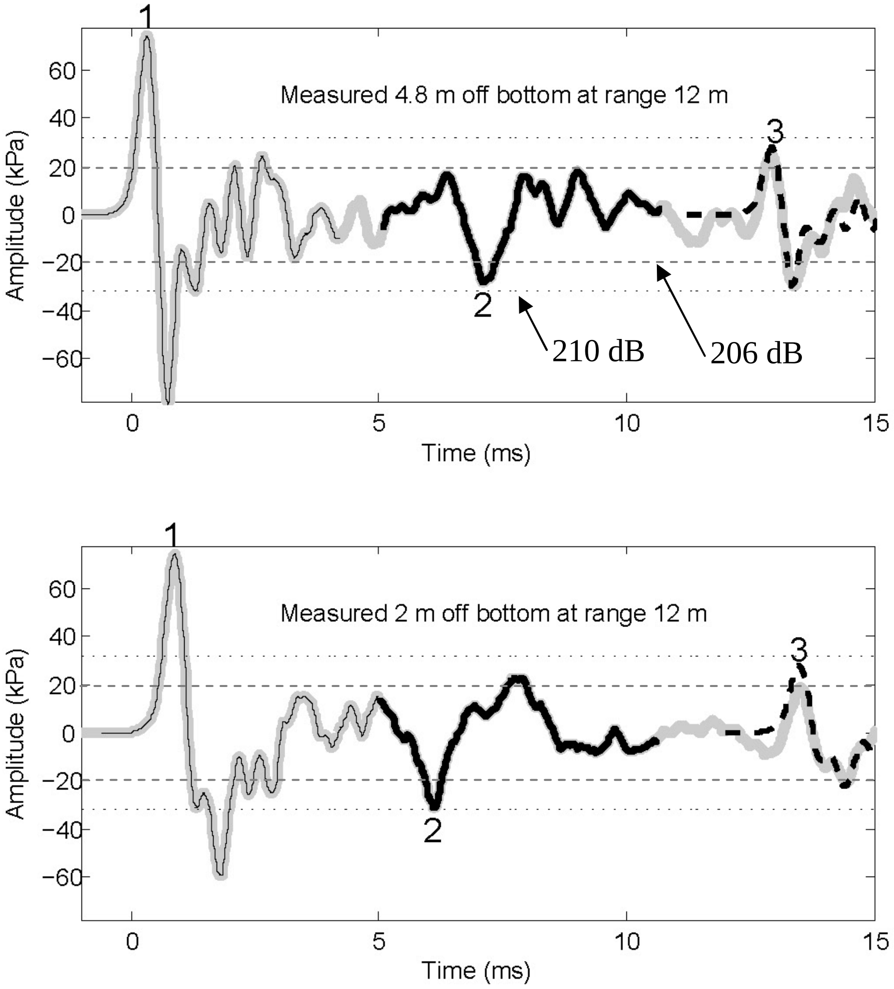

Figure 6. Pressure time series of underwater noise from impact installation pile driving measured at a range of 12 m at two heights above the bottom (gray lines). Horizontal dashed lines delineate peak positive or negative pressures exceeding 210 and 206 dB re 1 μPa. The pressure from the first and highest amplitude downward Mach cone (phase-1) is identified by the thin black line (label 1) plotted over the data for each receiver. The pressure from the first upward Mach cone (phase-2) is identified by the thick black line (label 2) also plotted over the data. A phase-3 is identified for each receiver by the dashed line, in this case representing a scaled version of phase-1 (amplitude reduction 3/8) delayed by 12.6 ms.

The scaling was determined by the bulge reflection coefficient at the bottom of the pile, $\alpha \approx -3/8$, which was estimated directly from the VLA data. That is, phase-2 was approximately an inverted phase-1 with an amplitude reduction of $|\alpha|$ = 3/8. As phase-3 originated from reflection from the top of the pile, it underwent a second inversion attributable to the strain relief boundary condition, and thus it reverted back to the same positive-to-negative pressure development as in phase-1 while maintaining anamplitude of 3/8 relative to phase-1 (i.e., no additional amplitude reduction). Finally, we anticipated a fourth phase associated with a second reflection from the bottom of the pile, with an amplitude reduction of $|\alpha|^2$ = 9/64 relative to phase-1. However, this 17 dB reduction made a fourth phase more difficult to identify in the data and distinguish it from the first three and more energetic phases.

Returning to the 12.6 ms T delay, it is interesting to see how this was also manifested in the energy spectral density. As seen in Figure 6, time delays between particular phases of the pulse arrival structure, e.g., between phase-1 and phase-2, depend on depth. But common to *all* depths is the T delay. Therefore, a depth-averaged energy spectral density (Figure 7) will reveal this delay in the form of spectral interference peaks every $1/T$ Hz or 79 Hz.

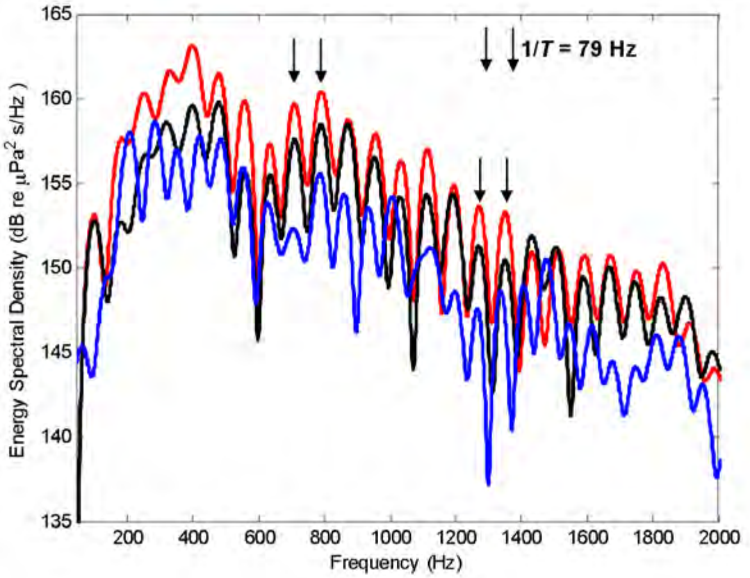

Figure 7. Energy spectral density depth averaged over the aperture of the VLA . Line color indicates the particular test and VLA range from the pile: 8 m (red), 12 m (black), and 15 m (blue). The spectra display prominent peaks separated by ~ 79 Hz.

The observable time lags seen in Figure 6 between measurements taken at different heights off the bottom can be associated with a vertical arrival angle. To estimate this angle, the least restrictive approach, from the standpoint of source and VLA far field criteria, is one based on the time lag estimate, $\hat{\tau}$, between adjacent sensors separated by L = 0.7 m. In Figure 8, eight pair-wise estimates of arrival angle, $\hat{\varphi}_w = a\sin(\hat{\tau}\, c_w / L)$, are plotted as a function of depth off the bottom for the three cases in which the VLA range was 8 m (red), 12 m (black), and 15 m (blue). The estimate of $\hat{\tau}$ was based on cross-correlation analysis of selected data segments, e.g., as indicated in Figure 6.

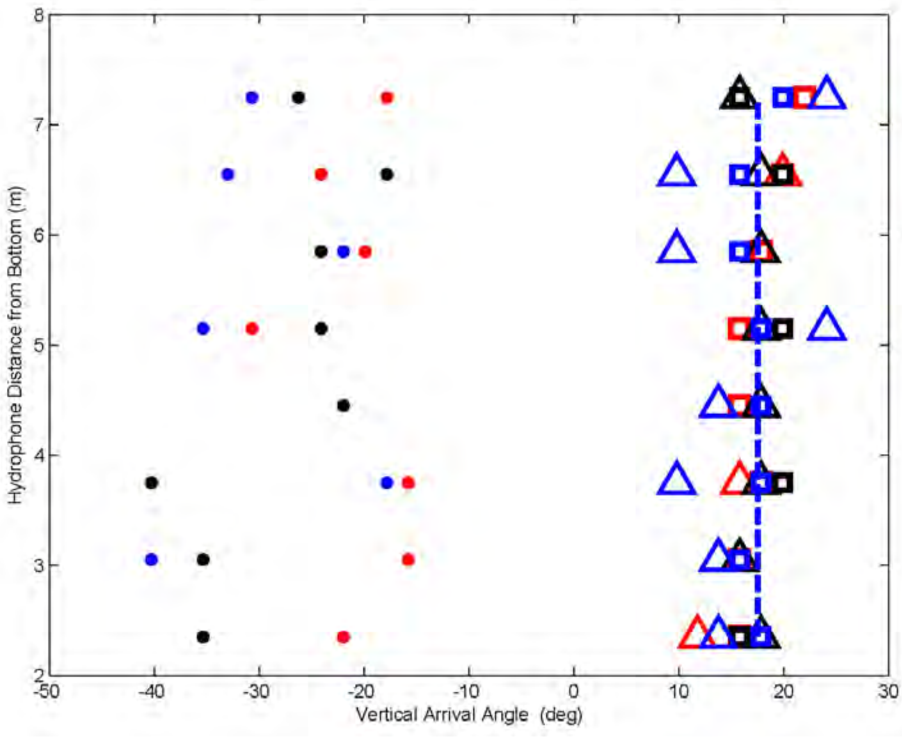

Figure 8. Estimated vertical arrival angle versus distance off the bottom for three pile driving measurement ranges. Symbol color indicates particular test and VLA range from the pile: 8 m (red), 12 m (black), and 15 m (blue). The abbreviations p1, p2, and p3 in the legend indicates time periods associated with phase-1, phase-2, and phase-3 segments, respectively, used in the estimation. The vertical line represents the mean of the phase-1 arrival angle estimates.

According to the FE results in Section 2.1, there are two opportunities to measure φ_w: one is phase-1 of the pulse (i.e., label 1, Figure 6) and the other, phase-3, is approximately T ~ 13 ms later, representing the field generated by the reflected bulge on the pile that has traveled twice the pile length (label 3, Figure 6). Estimates of φ_w cluster near 17.6^o (Figure 8, right side), a value equal to the mean of all the estimates derived from the first arrival, or phase-1 segment (p1 markers), which is close to the predicted value of 17.2^o. The estimated standard deviation is $\sim 2^o$, which is somewhat greater than the Cramer-Rao lower bound, as determined by signal bandwidth, signal-to-noise ratio (SNR), and mean arrival angle. Interestingly, the second set of estimates of φ_w (p3 markers) also clusters about the mean but with higher variance owing to a reduced SNR. An angle estimate from the first upward arrival (label 2, Figure 6) is also possible, with corresponding estimates shown on the left side of Figure 8 (p2 markers). These represent, in a sense, a combined estimate of φ_w (reversed in sign) and φ_{ws} (see Figure 4). This mixture of arrival angles, along with a lower SNR, necessarily results in a greater spread of estimates. It is significant that the arrival angle estimates do not vary, in a mean sense, with range over the three test ranges that span 0.75 to 1.25 water depths. This is consistent with a phased array of sources produced by the bulge on the pile traveling downward and upward at supersonic speed relative to the speed of sound in water.

2.3. Observations (2): Comparison with Parabolic Wave Equation Simulations

A broadband simulation of the received pressure pulse from impact pile driving was obtained through an inverse Fourier transform of a frequency-domain solution. For this, we used the RAM (Range-dependent Acoustic Model) PE code (Collins 1993) to compute the Green's function $G(\vec{r}, \vec{r}_i, f)$, representing the complex acoustic field at receiving position vector $\vec{r}$ and frequency f that originated from a unit-strength point source at $\vec{r}_i$. It was necessary to use multiple point sources distributed vertically over the wetted-length of the pile, as outlined further below, and to sum the results to obtain the desired acoustic field in the frequency domain. This field was computed for 1,024 frequencies between 50.8 Hz and 2048.8 Hz, every dF = 1.95 Hz, to accommodate a time spread of nominally 500 ms. Although the frequency-domain PE field was supported only up to ~2000 Hz, it was zero-padded up to 16000 Hz (8192*dF) before the Fourier transformation to the time domain to achieve a more refined interpolation in the time domain.

The geoacoustic model was a water column 12.5 m deep with a constant sound speed equal to 1485 m/s (measured at the time of the experiment with a conductivity-temperature-depth probe) and a sediment assumed to be a fluid halfspace (which was ultimately terminated by an artificially high absorbing layer (Jensen et al. 1994)). Boring logs from the site written before construction described a mixture of sand-like sediments. Although the FE analysis results discussed in Section 2.1 were based on a constant sediment speed, the longer propagation distances evaluated here may have been influenced by sound speed dispersion effects. Therefore, we used a model for sandy sediments (Williams et al. 2002) based on Biot theory for sediment sound speed as a function of frequency, which put the sound speed equal to 1600 m/s for the lower end of the frequency range and 1680 m/s for the upper end. For sediment attenuation, we used the empirical model (Zhou 2009) that was also consistent with Biot theory, which put attenuation between 0.002 and 1.325 dB/m for the lower and upper frequency limits. The density of the sediment was assumed to be 1.85 times that of the water column.

As suggested by both the FE analysis simulation and the field observations, the radial expansion, traveling down the pile at a speed of ~5000 m/s, and the ensuing Mach cone were responsible for the majority of the underwater sound energy observed. The PE simulations addressed only this feature by using a vertical distribution of time-delayed, broadband point sources, with a time delay of the i^{th} source located at $\vec{r}_i$ established by its vertical location and the speed of the pile bulge wave, c_p = 5048 m/s. This could also be viewed as a phased array of sources for which the phase was set by the supersonic speed of the bulge. (The speed was taken to be an average of the speeds in the water and sediment, although the latter was about 1 percent more, as discussed in Section 2.1.)

The PE implementation involved a distribution of 106 such point sources, at 0.25-m intervals, starting at the air-water interface and spanning the water column (12.5 m) and sediment phase (14 m) of the pile. To account for the pulse delay as the bulge travels down the pile, the received spectrum from the i^{th} point source, $s_i(\vec{r}, f)$, was computed as $s_i(\vec{r}, f) = G(\vec{r}, \vec{r}_i, f) A(f) e^{i 2\pi f \tau_i}$, where τ_i is the point source time delay equal to the source depth z_i divided by c_p, where z_i ranges from 0.25 m to 26.5 m and $A(f)$ is an empirical amplitude weighting spectrum. This spectrum was constructed from an estimate of the amplitude spectrum calculated by using isolated time segments associated with the first arrival, or phase-1 (e.g., as shown in Figure 6). Further details on the estimation procedure are provided below.

The complex amplitude spectrum of the first arrival, $S_1(\vec{r}, f)$, was the superposition of all the sources distributed over the wetted-length of the pile (water and sediment) as given by

$$S_1(\vec{r}, f) = \sum_{i=1}^{106} s_i(\vec{r}, f)\,. \qquad [1]$$

Convergence tests were applied with different source densities and spacing; for example, halving the number of sources to 53 with a spacing of 0.5 m provided the same answer, to within a calibration constant, as doubling the number of sources. The corresponding pressure field $p_1(\vec{r},t)$ was given by

$$p_1(\vec{r},t) = \mathrm{Re}\left[\int_{o}^{f\,\max} S_1(\vec{r}, f) e^{-i2\pi\, ft} df\right] \qquad [2]$$

(carried out with inverse FFT), where *f max* =16000 Hz, which is linked to the aforementioned zero-padding, as the actual support in the frequency domain is limited to about ~2000 Hz. The pressure field $p_1(\vec{r},t)$ represented a model for first arrival, or phase-1 of the data, as shown in Figure 6.

The complex amplitude spectrum of the second arrival, $S_2(\vec{r}, f)$, and third arrival, $S_3(\vec{r}, f)$, corresponding to phase-2 and phase-3 in Figure 6, were similarly constructed by using the summation of 106 sources as in Eq. (1). Here, time delays continued to accumulate as follows: for the second arrival the time delay, τ_i, for each source was

$$\tau_i = (P_{wl} - z_i)/c_p + P_{wl}/c_p\,, \qquad [3]$$

and for the third arrival the time delay was

$$\tau_i = 2P_l/c_p + z_i/c_p \qquad [4]$$

where total pile length, P_l , is 32 m, and wetted pile length, P_{wl}, is 26.5 m. For these two subsequent arrivals, the effect of amplitude and phase changes from pile-end reflections also had to be included in Eq.(1); therefore, for $S_2(\vec{r}, f)$ and $S_3(\vec{r}, f)$, Eq. (1) was multiplied by -3/8 and 3/8, respectively. These complex spectra were added to $S_1(\vec{r}, f)$ in Eq. (1) to obtain the total pressure field, $p(\vec{r}, t)$, or they could be inverse transformed separately to examine component fields. (Note that a $S_4(\vec{r}, f)$ associated with phase-4 could be similarly constructed, but its overall impact on the total field would be negligible, as in this case the multiplier would be -9/64.)

Returning to the amplitude spectrum $A(f)$, it was constructed from the data as follows: The first arrival was isolated from the three lowest hydrophone channels on the VLA (these were 2 m, 2.7 m and 3.4 m off the bottom). These channels were selected because of their higher SNR, allowing the first arrival, defined as the phase-1 segment of length 5 ms, as shown in the lower plot of Figure 6, to be more readily identified. Data from the 8-m range test were used, but results were similar for the 12-m and 15-m range tests. Before the FFT analysis, the segments were passed through an equal-length Tukey window (taper parameter, or ratio of taper to constant sections = 0.5) to smooth the transient effects associated with data truncation. An average of the magnitude-squared spectra from these three channels was taken, from which the square-root represented our estimate of the amplitude spectrum, $A(f)$, which was normalized to its maximum value. This spectrum was sub-sampled every 1.95 Hz to correspond to the PE frequencies, and it was further shaped (to a small extent) near its end points at 50.8 Hz and 2048.8 Hz by a Tukey window (taper parameter 0.015) to reduce a ringing effect in the time domain results. The final result (Figure 9) displayed the same approximate 10-dB decrease between the peak frequency near 300 Hz and 2000 Hz, as shown in Figure 7, but without the frequency interference effects shown with the latter owing to the 12.6-ms time delay.

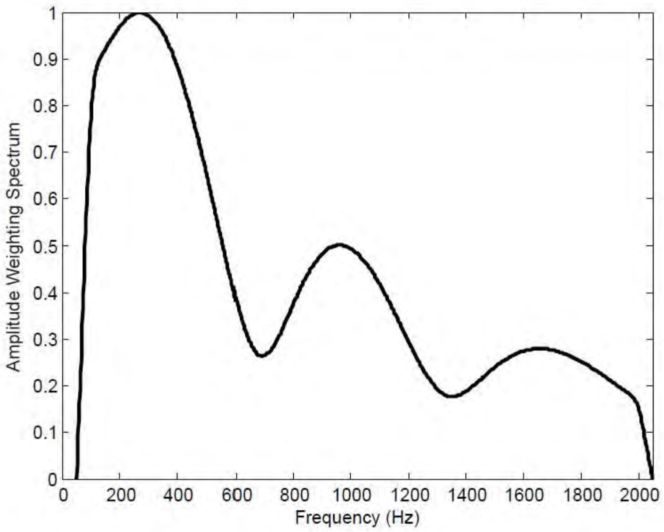

Figure 9. The amplitude weighting spectrum *A(f)* used for the PE analysis that was estimated from data (see text for estimate procedure). Note that *A(f)* is defined every 2 Hz between 50 and 2050 Hz.

Figure 10 shows a comparison between measured first-arrival pressure amplitude as a function of hydrophone depth and range and its PE-simulated counterpart for the three ranges measured: 8 m, 12 m, and 15 m. The simulated results for all ranges were given the same *single* calibration offset, 232 dB, which applied to all depths and was derived from a least squares fit between the simulated data and the corresponding 27 observations representing nine depths and three ranges. (With convergence testing, this offset would be exactly 6 dB higher if half the number of sources, i.e., 53, were used.) Note that each observation in Figure 10 has a spread of at least +/- 1.5 dB owing to calibration uncertainty. Also important is the apparent clustering of both the data and simulation results at all ranges to within about 2 dB to 3 dB at the lowest hydrophone depth (10.5 m, or 2 m above the bottom) and the corresponding spread at these ranges of about 8 dB at the shallowest depth (5 m, or 7.6 m above the bottom).

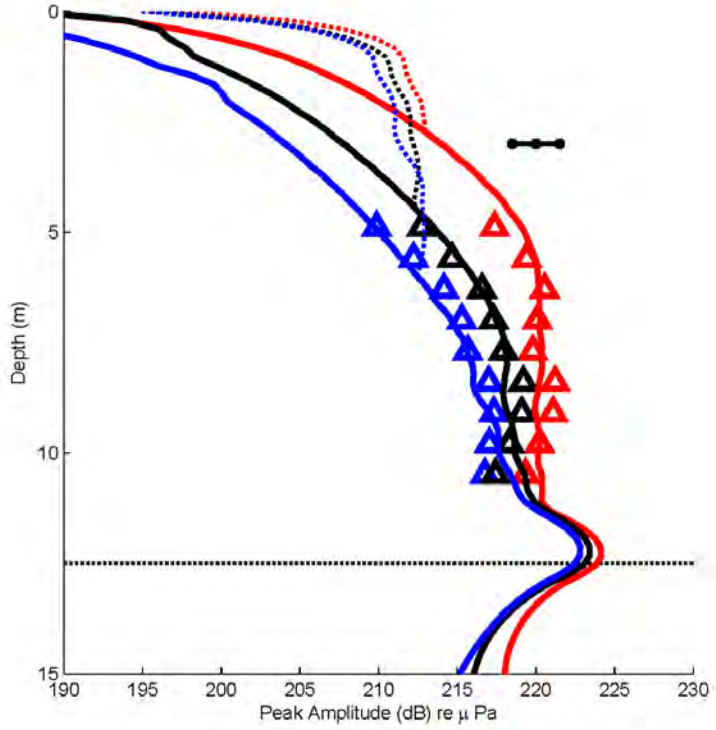

Figure 10. Measurements (symbols) of the first-arrival pressure amplitude, expressed in dB re 1 μPa as a function of hydrophone depth and range, representing the three measurement ranges: 8 m (red), 12 m (black), and 15 m (blue). A representative error spread is shown in upper left. The solid thick lines with the same color coding show PE-simulated counterpart based on a phased-array of sources as described in the text. Note that for the measurements, the first-arrival amplitude coincides with the peak amplitude. The thin dashed lines with the same color coding show a PE-simulated peak pressure amplitude, which coincides with the first-arrival amplitude for depths below D^*. The horizontal dotted line delineates the water sediment interface at a depth of 12.5 m.

For all observations at the three ranges, the pressure amplitude of the first-arrival coincides with the peak amplitude, and these observations agree well with the PE-simulated first-arrival (solid lines in Figure 10). It is interesting to examine the PE-simulated *peak* amplitudes (dotted lines in Figure 10), which begin to differ from the first-arrival amplitudes at depths of above D^*; this depth represents the approximate boundary of the first and primary Mach cone (see Section 2.1). However, fully capturing this interesting feature of the pressure field with the limited number of VLA sampling depths and ranges is more difficult. Although, it was not explicitly verified with data from our particular field geometry, Figure 10 suggests that the maximum pressure levels will continue to be observed near the water-sediment interface out to ranges of a few depth scales. Finally, a comparison between the PE-simulated and measured time series at 12 m (Figure 11) shows reasonable agreement over the duration of the time series. (It is represented as the absolute value of the Hilbert transform of both data and simulation, and the same calibration offset, 232 dB, was applied to the latter.) To help in visualizing the time delays, a dot is placed below the peak of the first arrival in the pressure data for each channel, and a second dot is located on the graph exactly 12.6 ms later. The first dot nominally traces the arrival time of the downward Mach cone, and the second dot traces its repetition occurring 12.6 ms later, as discussed in the context of figures 6 and 7. Evidence for the upward Mach cone, more difficult to track, can be seen in the data within the 6 ms to 8 ms time window in the deepest channel and within the 8 ms to 10 ms time window in the most shallow channel.

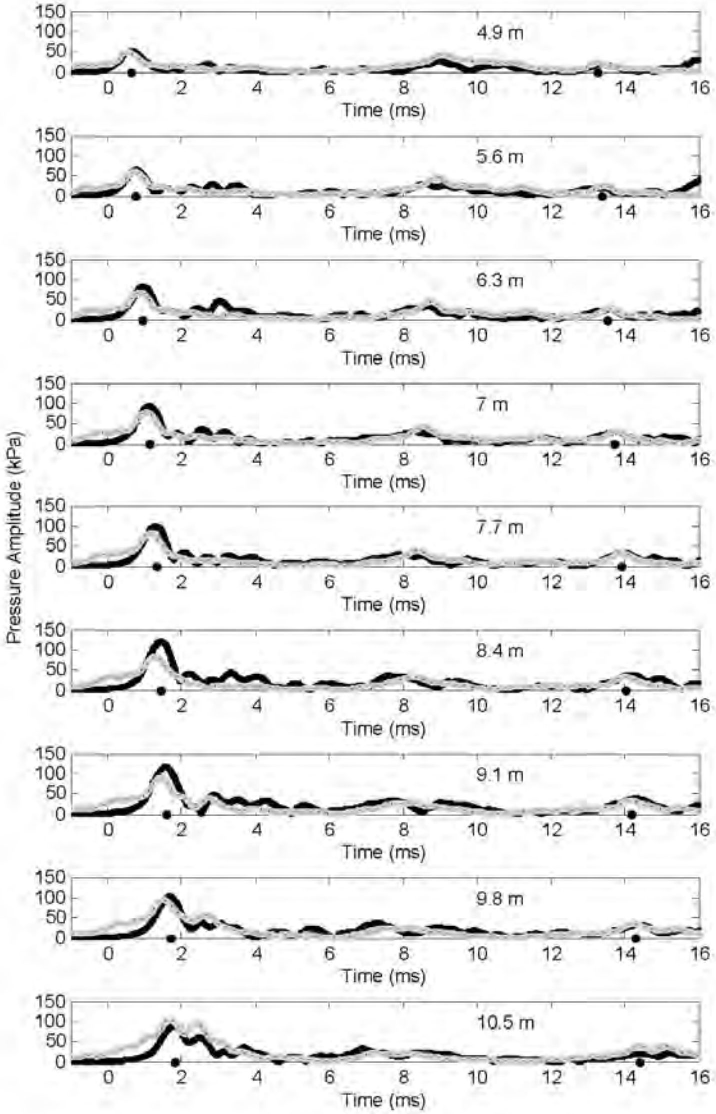

Figure 11. Comparison between measured (black lines) and PE-simulated (gray doted lines) time series for the nine elements of the VLA at a measurement range of 12 m. Element depth is noted in each case. For the measured data, the arrival time for first and maximum arrival at each depth is identified by the black dot (left side), and a second black dot is plotted 12.6 ms after this time (right side).

3. NOISE ATTUNATION USING A TEMPORARY NOISE ATTENUATION PILE

The effectiveness of a Temporary Noise Attenuation Pile (TNAP) at reducing the underwater sound caused by pile driving operations was also evaluated during the 2009 Vashon ferry terminal dolphin replacement project. To this end, a 48-ft-long, double-wall TNAP was constructed by using two concentric pipes with outside diameters of 60 and 48 in. and a wall thickness of 1 in. (see Figure 12). The 5-in. space between the inner and outer steel tubes was partially filled with a 4-in.-thick, sound absorbing material. Bubbles between the pile and the hollow tube were introduced though a bubble ring at the bottom of the TNAP.

To test the effectiveness of the TNAP, four 105-ft-long, 30-in.-diameter piles were driven 35 feet into the sediment with a vibratory hammer. The TNAP was then installed (see Figure 13) around the pile, and the pile was driven another 8 to 9 ft by using a Delmag D62-22 Diesel Hammer with an impact weight of 6,200 kg and energy of 180 kNm, as specified in Section 2.1. The last foot was driven with the TNAP removed, and data were collected for the untreated pile (Section 2). This procedure was repeated for four piles. A schematic of the TNAP concept is shown in Figure 14.

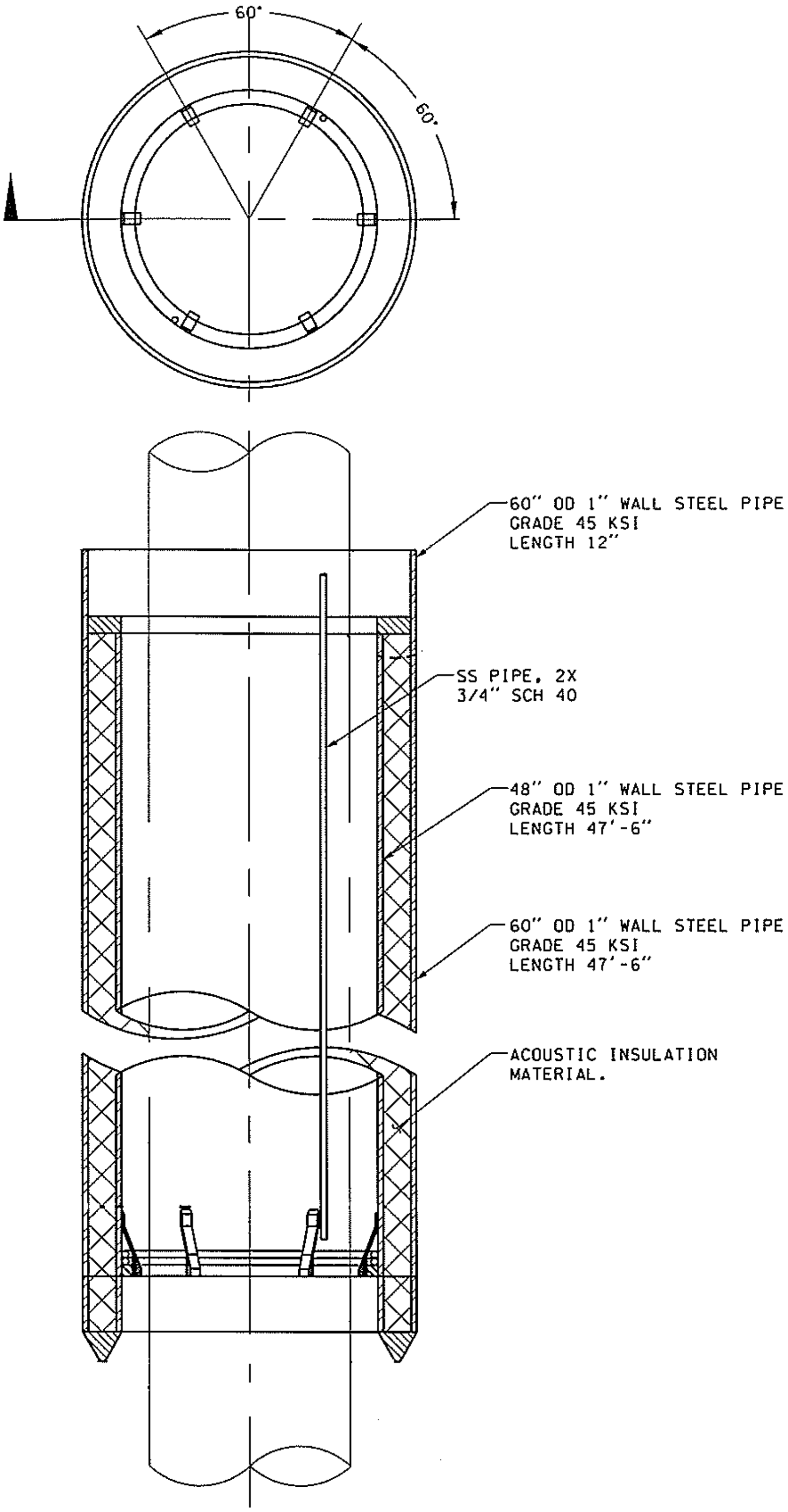

Figure 12. Sketch of the TNAP

Figure 13. Installation of the TNAP around a 30-in.-diameter pile.

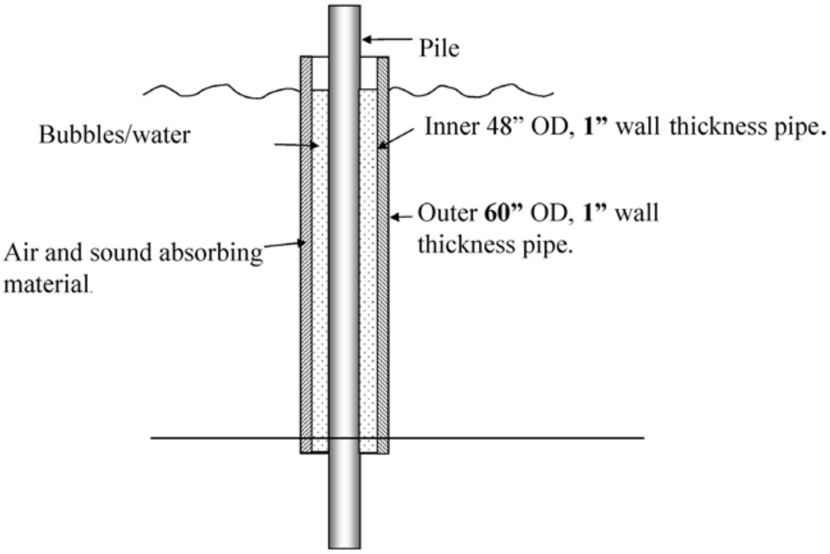

Figure 14. Schematic of the TNAP concept

3.1 Modeling Results

To investigate the acoustic radiation due to a pile strike when the pile was surrounded by a TNAP, we complemented the finite element model discussed in Section 2.1 with a detailed finite model of the TNAP. All significant components of the TNAP were modeled, including the two pipes, the sound absorbing material, the bottom steel ring, and the flexible top connection.

Figure 15 shows an axisymmetric surface plot of the total acoustic pressure at 5, 8, 11, 13, and 17 ms after impact. The figure shows that the TNAP was very effective at attenuating the noise produced by the part of the pile that was submerged in the water. A significant Mach cone was not produced until the compression wave and the associated radial bulge reached the sediment surrounding the TNAP. The radial deformation in the pile and the apex of the Mach cone, then contained within the sediment only, reached the bottom end of the pile approximately 6 ms after impact. As for the untreated pile, an upward moving Mach cone was produced after the first reflection of the structural wave. At approximately 8 ms the structural wave and the apex of the upward moving Mach cone reached the TNAP and the water-sediment interface. The pile bulge again propagated inside the TNAP, and the creation of the Mach cone was essentially stopped. As can be seen in Figure 14, the upward moving Mach wave that was produced in the sediment reached the water-sediment after 8 ms and continued to propagate up into the water.

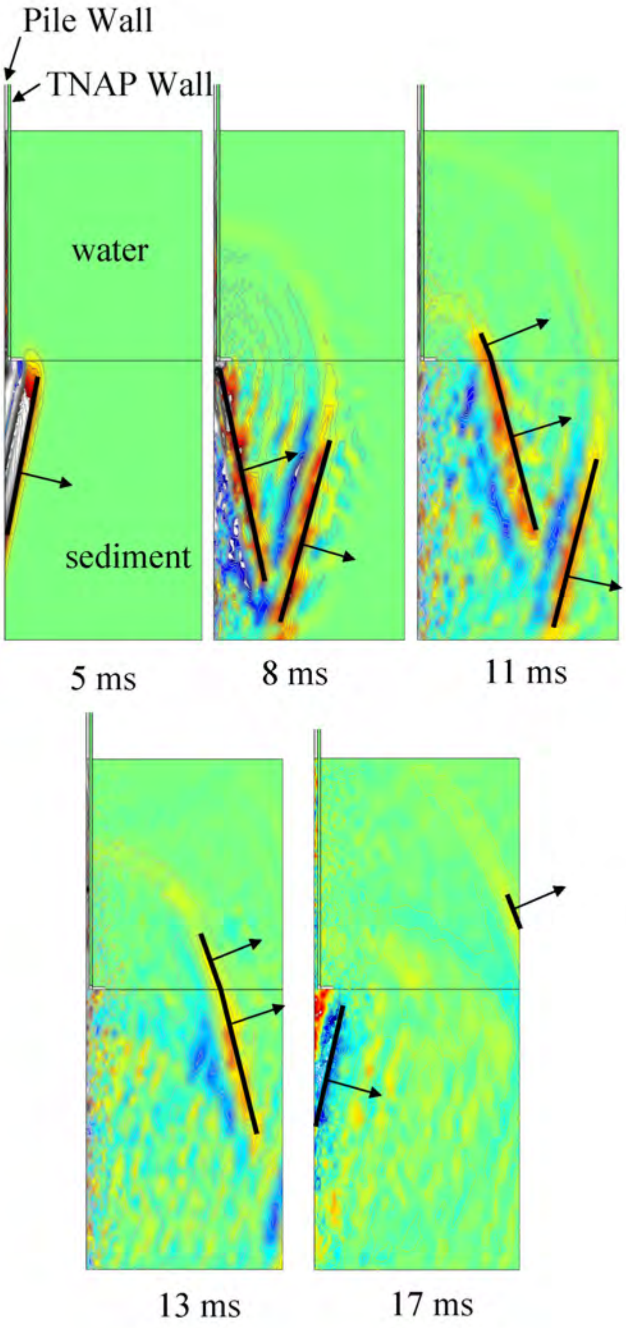

Figure 15. Acoustic pressure surface plots showing the acoustic radiation from the pile with the TNAP after 5, 8, 11, 13, and 17 ms after impact by pile hammer. The propagation directions of the wave fronts associated with the Mach cones produced in the water and the sediment are indicated by the arrows.

A schematic of the FE analysis results is shown in Figure 16 \ to clarify the chain of events and compare the process to that of the untreated pile case. Figure 16 shows that the first Mach cone is formed with a cone angle of $\varphi_s = \sin^{-1}(c_s / c_p) = 18.6^\circ$. As for the untreated case, this is the angle between the vertically oriented pile and the wave front associated with the Mach cone. As the deformation wave is reflected against the bottom end of the pile, the reflection produces an upward moving Mach cone of angle φ_s. The sound field associated with this cone propagates up through the sediment and penetrates into the water, whereupon φ_s changes to $\varphi_{ws} = 30.0^o$ following Snell's law. Essentially, no Mach cone is produced by the upward moving pile wave front in the water. FE analysis predicts that the TNAP attenuates the sound field produced directly by the interface between the pile and the water more than 30 dB. However, the TNAP, because of its limited coverage, does nothing to decrease the Mach cone emanating from the sediment into the water.

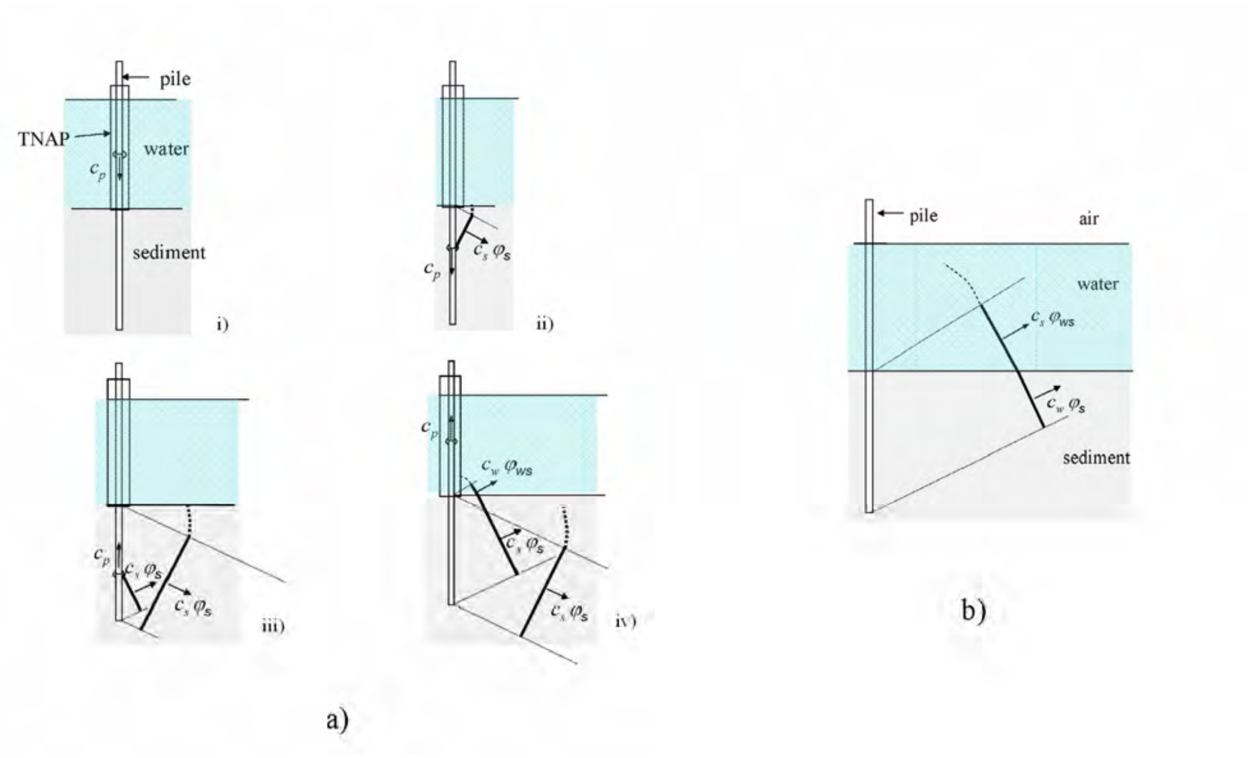

Figure 16. (a) Illustration of the propagation of the primary wave fronts associated with the Mach cone generated by the pile compression wave when the pile is surrounded by the TNAP. i) Wave fronts before reaching the sediment. ii) Wave frontss after the pile deformation wave hasve reached the sediment. iii) Wave fronts after the first reflection of the deformation wave. iv) Wave fronts after the reflected deformation wave has reached the water.
(b) Illustration showing only the first upward traveling wave fronts after the deformation wave has reached the top of the pile.

3.2 Field Test Results

As described in Section 2, acoustic data were recorded at a sample rate of 62,500 Hz with a hydrophone receiving sensitivity equal to -210 dB re V/μPa (+/- 1.5 dB), without pre-amplification to avoid system network saturation from the expected high-level inputs. Figure 17 shows the acoustic pressure originating from an untreated pile (black line) and a pile surrounded by a TNAP (grey line) as recorded by a hydrophone in the VLA located 4.8 m off the bottom at a range of 12 m. In both cases the pile was driven by a 6,200 kg impact hammer with an energy of 180 kNm. For reference, the horizontal dotted lines show where the pressure amplitude exceeded 210 dB re 1 μPa.

Figure 17 shows that the pressure recording for the TNAP totally lacked the initial pulse of the untreated pile that was associated with the first arrival of the downward moving Mach cone (which reached 215 dB re 1 μPa). This Mach cone was created in the untreated case by the direct interaction between the pile and the water. The negative spike at approximately 8 ms existed for both the TNAP and the untreated case and corresponded to the arrival of the upward moving Mach cone that was created in the sediment after the first reflection of the pile bulge. This wave was not hindered by the TNAP because the TNAP did not reach down into the sediment. This spike limited the effectiveness of the TNAP, since it resulted in a peak amplitude pressure of 204 dB re 1 μPa, or 11 dB less than the maximum peak pressure for the untreated pile. (This difference actually ranged from 10 dB to 15 dB, depending on the case study, as will be discussed at the end of this section.) Note that a weaker spike in the TNAP pressure data existed at 3.5 ms, or 4.5 ms before the arrival of the Mach cone. This spike was due to a wave diffracted into the water when the initial downward moving pile bulge wave left the TNAP. In Figure 15, this wave takes on a circular shape and connects with the first downward moving Mach cone at the water/sediment interface.

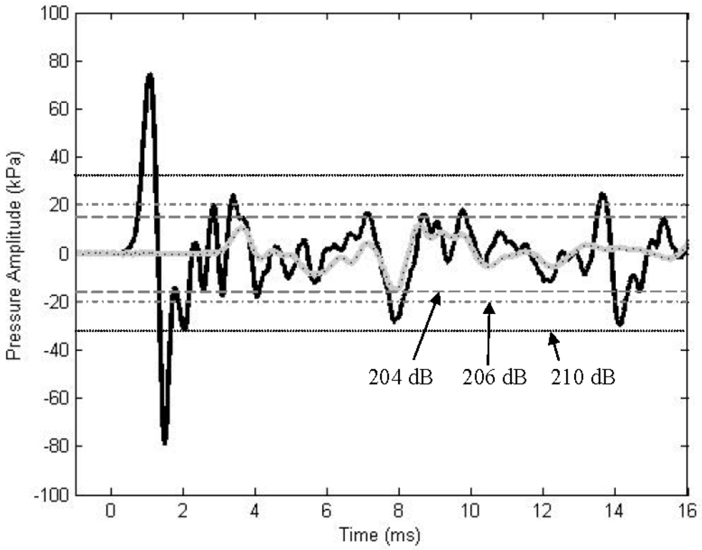

Figure 17. Acoustic pressure originating from an untreated pile (black line) and a pile surrounded by the TNAP (grey line) as recorded by a hydrophone in the VLA located 4.8 m off the bottom at a range of 12 m.

Figure 18 show the acoustic pressure records from all nine hydrophones at a range of 12 m. The black dotted line connects the maximum amplitude peak recorded by all the hydrophones. The slope of this line shows that the Mach wave arrived at the lowest hydrophone first. The angle of the upward moving Mach wave was estimated from the measured data to be equal to 34^o. This is clear experimental confirmation of the modeling results presented in the previous section. The small error in the angle of the Mach cone is most likely due to a difference between the actual and estimated wave speed in the sediment.

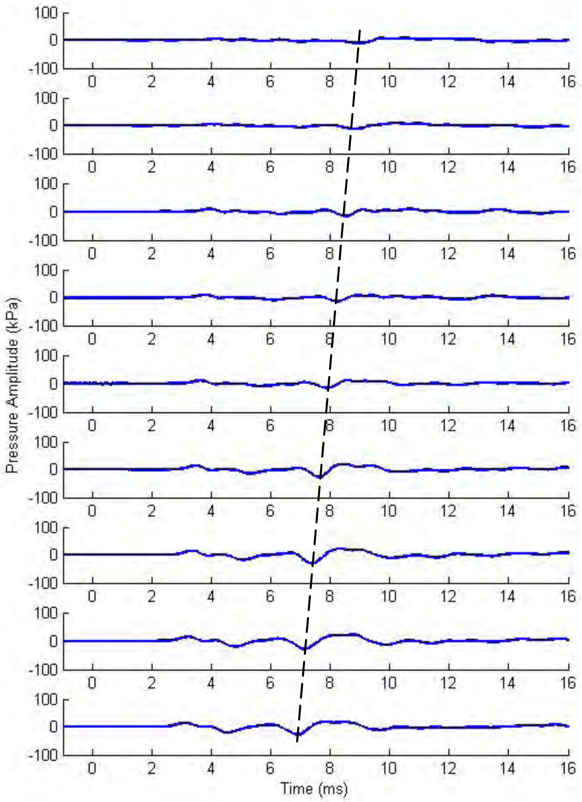

Figure 18. The acoustic pressure records from all nine hydrophones at a range of 12 m. The black dotted line connects the maximum amplitude peak recorded by all the hydrophones. The slope of this line shows that the Mach wave arrived at the lowest hydrophone first.

Figure 19 summarizes all measurements of the untreated piles and the TNAP piles at the three ranges during the Vashon test. The differences in the peak pressures between the untreated and TNAP piles varied somewhat as a function of test range and depth of measurement, but they were consistently between 10 dB and 15 dB. On the other hand, the differences for single strike Sound Exposure Level (SEL) were somewhat less, say 5 to 10 dB. This is understandable in view of the way that the TNAP system effectively blocked the first and peak arrivals but not later arrivals that originated from the seabed, which all contributed to the SEL.

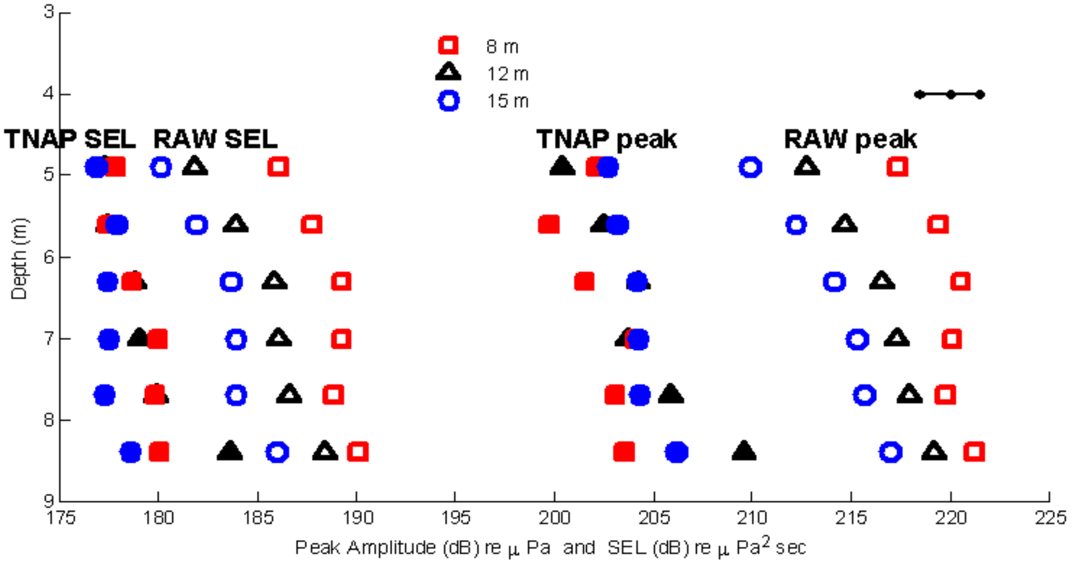

Figure 19. Summary of peak acoustic pressure and SEL for raw pile and TNAP pile measurements at Vashon at ranges of 8, 12, and 15 m versus depth. The error bar in the upper right corner applies to each data point.

4. TRANSMISSION LOSS FROM VIBRATORY PILING

This section presents findings from an investigation of the transmission loss from a vibratory piling test off the Port Townsend Ferry dock conducted in October 2010.

4.1. Data Analysis

Figure 20 shows a histogram of short-time-averaged values expressed in dB of the signal centered at 1000 Hz produced by vibratory pile driving measured at range 10 m. The key point is that when such data are processed in order to vary narrow bandwidths, the range of variation is not only quite large (~20 dB) but also very predictable. The theoretical prediction can be found in Dahl and Plant (1997), which gives a standard deviation of 5.6 dB.

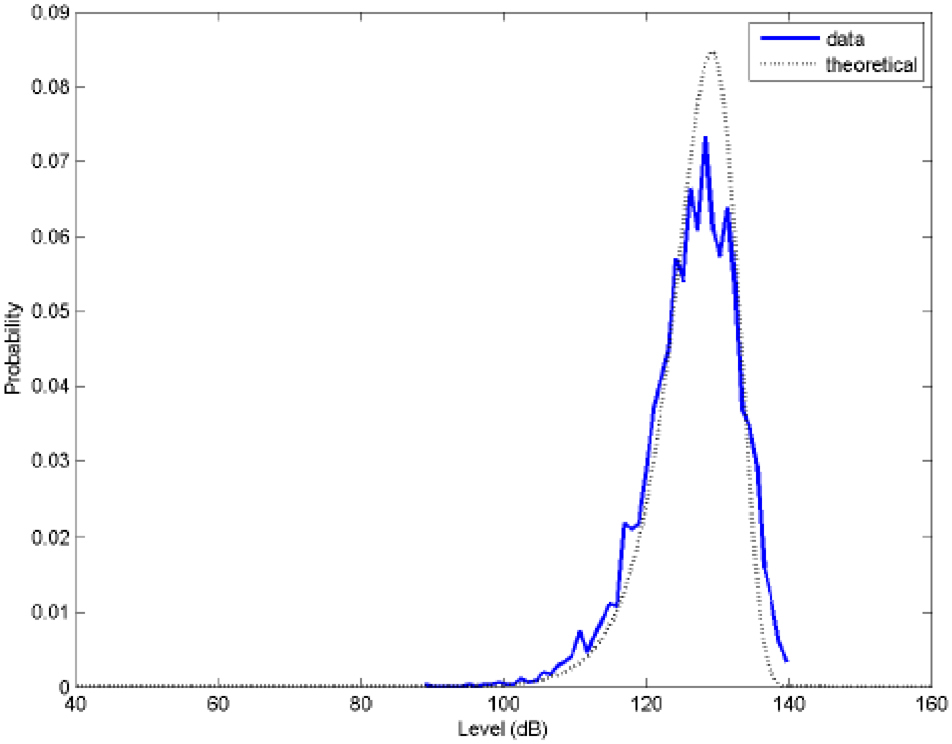

Figure 20 Narrow band received level in dB re 1 μPa, center frequency 1000 Hz, for vibratory pile driving measured at a range of 10 m.

In Figure 21, a similar histogram of short-time-averaged values made from the same signal, but at a range 3200 m), is governed by the same probability density function.

Transmission loss between 10 m and 3200 m is the decibel ratio of the two mean-square pressures involved, or equivalently, decibel subtraction of the data in Figure 20 from those shown in Figure 21. The resulting transmission loss histogram is shown in Figure 22 has a theoretical standard deviation of $\sqrt{2}$ 5.56 dB.

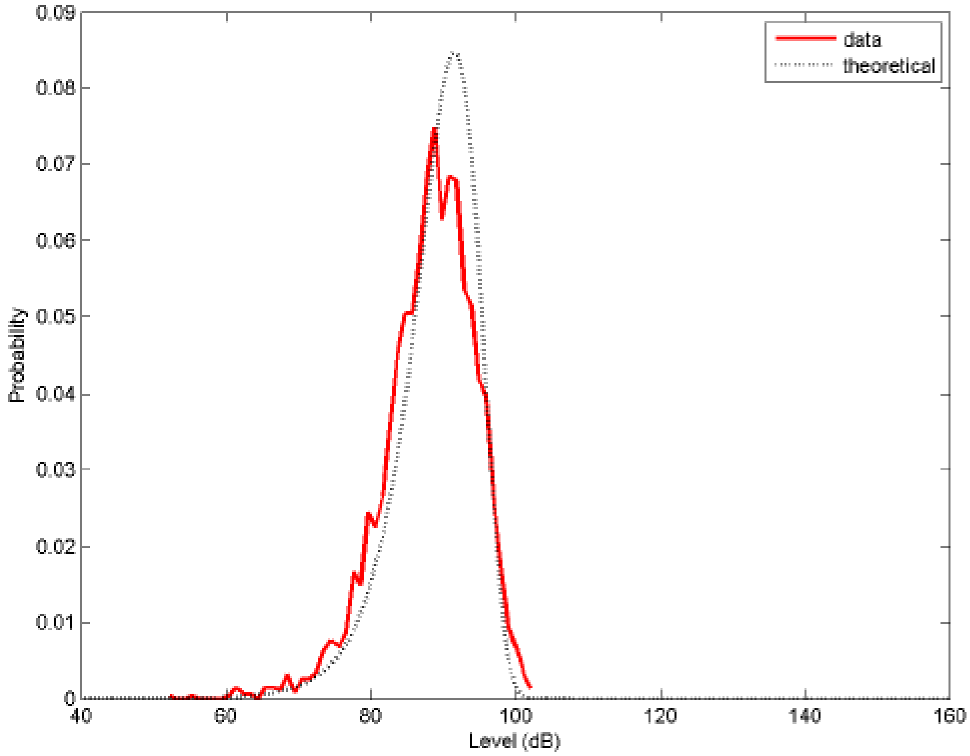

Figure 21. Narrow band received level in dB re 1 μPa, center frequency 1000 Hz, for vibratory pile driving measured at a range of 3200 m.

The key message from this study is that transmission loss is inherently quite variable, a fact that should be considered in studies that involve only a few observations.

That said, the nature of this variation can be both understood and predicted, with results that could help agencies make better use of their monitoring resources. In the next section we address this briefly by using state of the art acoustic modeling techniques.

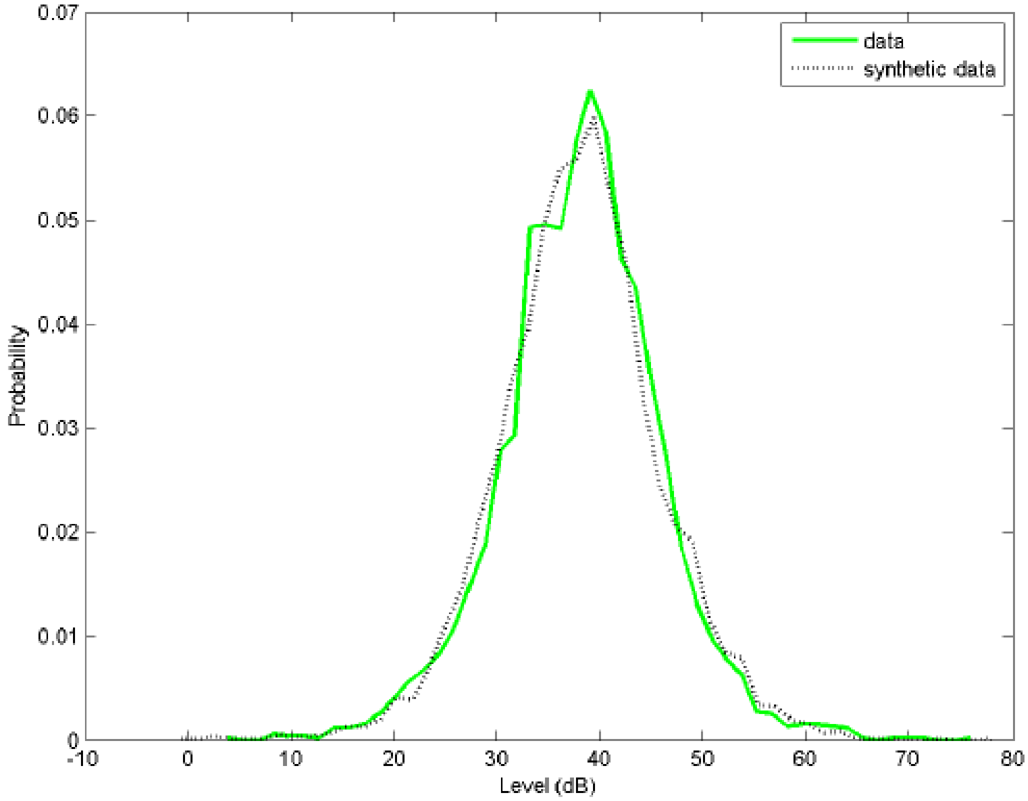

Figure 22. Histogram of narrow band transmission loss between range 10 m (Figure 19) and 3200 m (Figure 20), in comparison with theoretical values.

4.2. Studies Using the Parabolic Wave Equation

The Port Townsend environment also showed considerable variation in bathymetry. This variation has an impact on the prediction of mean transmission loss, as is readily seen in Figure 23. For example, depth-averaged transmission loss (red line, Figure 24) occasionally follows the so-called PSM, or Practical Spreading Model (yellow line, Figure 24) but also frequently differs from the PSM by 10 dB or more. This typically happens in areas associated with large changes in bathymetry. Other factors, such as sediment type (e.g., hard rock, sand, or muddy sediments) affect the overall transmission loss, and this, along with bathymetry, needs to be included in the modeling. The result of better modeling will be more effective use of monitoring resources.

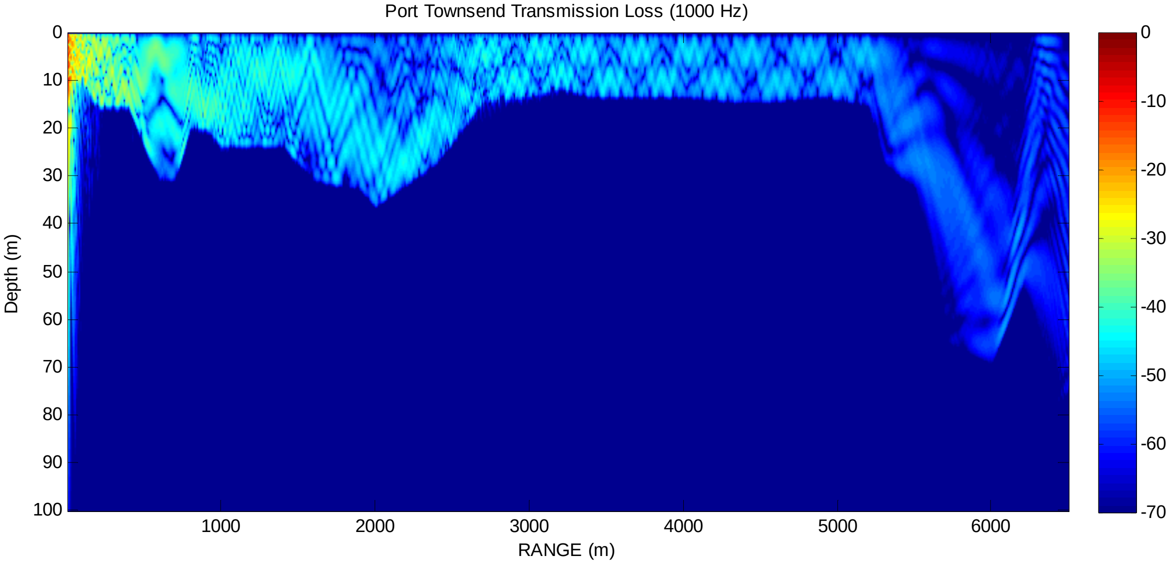

Figure 23. Transmission loss versus range and depth for the Port Townsend range based on available bathymetry and computed with the parabolic wave equation.

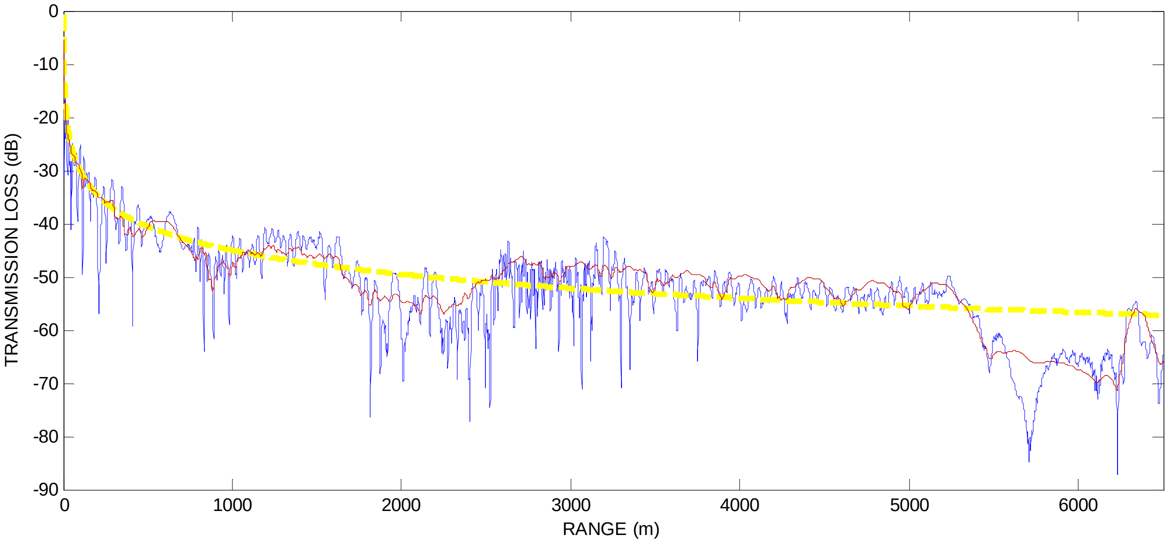

Figure 24. Transmission loss versus range at one depth 7 m (blue), depth average 0-10 m (red), and practical spreading model (yellow). The blue and red lines are derived from the results shown in Figure 23.

REFERENCES

Collins, M.D. “A split-step Padé solution for the parabolic equation method,” J. Acoust. Soc. Am. 93, 1736-1742, 1993.

Dahl P.H., and W. J. Plant, The variability of high-frequency acoustic backscatter from near the sea surface, ***J. Acoust. Soc. Am***., 101 (5), 2596-2602, May 1997.

de Jong, C.A.F and M.A. Ainslie, “Underwater radiated noise due to the piling of the Q7 Offshore Wind Park,” In: Proceedings of the European Conference on Underwater Acoustic, Acoustics ’08, M. Zakharia (ed), Paris, France, pp. 117-122, 2008.

Fellenius, B.H. ”Reflections on pile dynamics”, Keynote paper to the 5th Int. Conf. on the Application of Stress-Wave Theory to Piles, Orlando, 1996.

Jensen, F.B., W.A. Kuperman, M. B. Porter , and H. Schmidt, Computational Ocean Acoustics, American Institute of Physics, New York, 1994.

Madsen, P.T., M. Wahlbert, J. Tougaard, K. Lucke and P. Tyack, “Wind turbine underwater noise and marine mammals: implications of current knowledge and data needs,” Marine Ecology Progress Series, Vol. 309: 279-295, 2006.

Robinson, S.P., P. A. Lepper, and J. Ablit , “The measurement of the underwater radiated noise from marine piling including characterization of the a ‘soft start’ period,” In: Proceedings IEEE Oceans 2007, IEEE cat. 07EX1527C, ISBN: 1-4244-0635-8, 061215-074, Aberdeen, June 2007.

Weston, D.E. “Underwater explosions as acoustic sources,” Proc. Phys. Soc. 76: 233, 1960.

Williams, K.L., D. R. Jackson, E. I. Thorsos, D. Tang, and S. G. Schock, “Comparison of sound speed and attenuation measured in a sandy sediment to predictions based on the Biot theory of porous media,” IEEE J. Ocean. Eng. 27, 413-428, 2002.

Zhou, J., X. Zhang, and D. P. Knobles, “Low-frequency geoacoustic model for the effective properties of sandy bottoms,” J. Acoust. Soc. Am. 125, 2847-2866, 2009.